Catalyst-proximal plastrons enhance activity and selectivity of carbon dioxide electroreduction

Cell Reports
Physical Science

CellPress
OPEN ACCESS

Article

Catalyst-proximal plastrons enhance activity and selectivity of carbon dioxide electroreduction

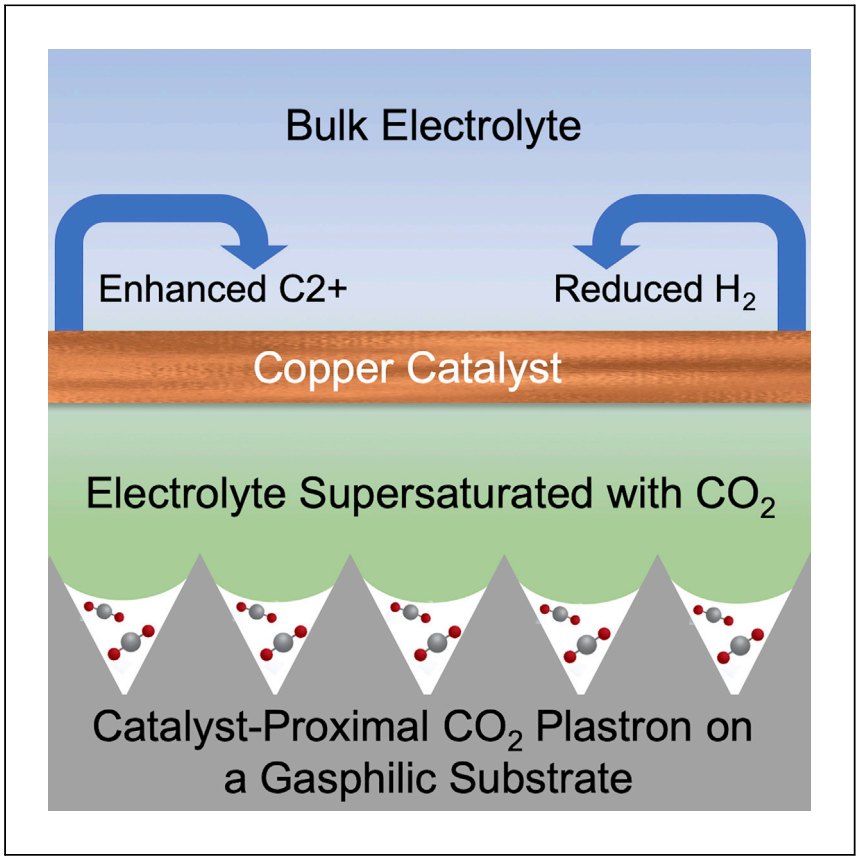

Khan et al. report how bubble-capturing surfaces can enhance electrocatalytic reduction of CO_2 by local supersaturation of CO_2 in the electrolyte near the catalyst, overcoming mass transport limitations. Thereby, hydrogen co-evolution is suppressed and formation of attractive C2+ products, such as ethanol and ethylene, is increased.

Sami Khan, Jonathan Hwang, Yang-Shao Horn, Kripa K. Varanasi

shaohorn@mit.edu (Y.-S.H.)
varanasi@mit.edu (K.K.V.)

HIGHLIGHTS

Gasphilic surfaces capture CO_2 bubbles

Local CO_2 concentration proximal to copper catalyst becomes supersaturated

CO_2 electroreduction current density is enhanced and maintained throughout the reaction

Hydrogen Faradaic efficiency is suppressed and C2+ product formation is enhanced

Khan et al., Cell Reports Physical Science 2, 100318
February 24, 2021
https://doi.org/10.1016/j.xcrp.2020.100318

Cell Reports
Physical Science

CellPress
OPEN ACCESS

Article

Catalyst-proximal plastrons enhance activity and selectivity of carbon dioxide electroreduction

Sami Khan,[1] Jonathan Hwang,[2] Yang-Shao Horn,[3,*] and Kripa K. Varanasi[3,4,*]

SUMMARY

Electrochemical reduction of carbon dioxide (CO_2RR) is an attractive approach toward converting CO_2 to solar fuels. Novel catalyst chemistries and morphologies may provide high selectivity to both one-carbon (C1) and two-carbon (C2) products over hydrogen; however, the limited aqueous solubility of CO_2 restricts the CO_2RR current density. Here, we demonstrate how gasphilic bubble-trap surfaces enhance mass transfer and enrich and maintain CO_2 concentration during CO_2RR by forming a catalyst-proximal plastron layer, consequently increasing the CO_2RR activity on both smooth and nanostructured copper as compared to the conventional headspace or bubbling modes of CO_2 delivery. The H_2 Faradaic efficiency is suppressed from 33% to 13% on smooth copper and from 62% to 33% on nanostructured copper, accompanied by enhanced formation of C2+ products, including ethylene, propanol, and ethanol, and >1% acetone and acetate. We highlight the importance of the catalyst-proximal plastron approach by comparing against recent aqueous-phase CO_2RR studies.

INTRODUCTION

Over the past several years, the concentration of CO_2 in the Earth's atmosphere has risen at an alarming rate, thereby causing an increase in global temperatures owing to the greenhouse effect. Numerous approaches have been proposed to tackle growing CO_2 levels: from minimizing consumption of fossil fuels to capturing and sequestering CO_2. Although these are promising avenues, CO_2 conversion in particular is attractive, as it has the potential to provide useful end products.[1,2] Electrochemical reduction of CO_2 (CO_2RR) is one approach toward converting CO_2 to synthetic or solar fuels, where much research has been focused on developing novel catalysts to enhance the kinetics (activity) and product distribution (selectivity).[3-8] Copper has been studied extensively, as it can produce hydrocarbons with both one carbon (C1), such as methane, and two carbons (C2), such as ethylene, in addition to oxygenates, such as formate, ethanol, and n-propanol.[4,9] Recent studies have shown increased geometric current density or selectivity toward C2 products on copper by using nanostructures,[10-13] controlling surface crystallinity,[14-16] and utilizing gas diffusion electrodes.[17,18] Unfortunately, copper is not immune from the competing hydrogen evolution reaction (HER). The poor solubility of CO_2 in water (~34 mM saturation concentration at ambient conditions)[19] limits the CO_2RR current density, and HER is favored if the aqueous CO_2 concentration becomes locally undersaturated close to the catalyst during CO_2RR.[20] This limitation becomes even more significant for nanostructured copper, because the increased active surface area leads to faster depletion of local CO_2, thereby promoting HER and reducing CO_2RR.[21-23] Hence, overcoming these mass transport limitations can enable higher CO_2RR activity while reducing HER.

[1]School of Sustainable Energy Engineering, Simon Fraser University, Surrey, BC V3T 0C5, Canada

[2]Department of Materials Science and Engineering, Massachusetts Institute of Technology, Cambridge, MA 02139, USA

[3]Department of Mechanical Engineering, Massachusetts Institute of Technology, Cambridge, MA 02139, USA

[4]Lead Contact

*Correspondence: shaohorn@mit.edu (Y.-S.H.), varanasi@mit.edu (K.K.V.)

https://doi.org/10.1016/j.xcrp.2020.100318

Here, we develop a gasphilic CO_2 trap that is placed in close proximity to the catalyst (see Figure 1C) that enhances gas-liquid mass transfer and maintains supersaturated CO_2 concentration around the catalyst during CO_2RR. Gasphilic surfaces require a special combination of surface chemistry and texture to capture bubbles and form a sheet of gas underwater also known as plastron.[24,25] By creating hierarchical micro-nano pyramidal textures on silicon (see Experimental Procedures and Figure S3), CO_2 bubbles are efficiently captured (see sequential high-speed camera images in Figure 1F and Video S1) within the textures, thereby forming a CO_2 plastron that appears silvery as shown in Figure 1D. When this CO_2 plastron is placed close to a smooth, electropolished Cu wire during CO_2RR (~3 mm distance), the current density is enhanced and sustained throughout the experiment at -1.1 V_{RHE} when compared to two commonly used methods of CO_2 delivery: headspace and bubbling in the bulk electrolyte (see Figure 1J and Experimental Procedures for detailed description of the electrochemical setup and conditions and Figures S1 and S2). We also find that the HER Faradaic efficiency does not appreciably change over time for the plastron and is greatly reduced (~13%) compared to that of the headspace (~33%) and bubbling (~29%) approaches. By trapping gas bubbles and spreading the gas into a sheet, the gasphilic surface has the unique ability to increase gas-liquid interfacial area and residence time. This allows for rapid replenishment of CO_2 during the CO_2RR reaction and prevents any depletion of CO_2 concentration in the vicinity of the catalyst.

RESULTS

CO_2 concentration enhancement

To confirm that the enhancement in CO_2RR activity and selectivity was indeed arising from the enriched CO_2 concentration close to the catalyst, we used two sensitive pH microprobes to track the aqueous CO_2 concentration in the electrolyte both near the plastron (~2 mm) and in the bulk during CO_2RR (4 cm from the catalyst surface). The aqueous CO_2 concentration can be determined from the measured pH using the following equilibria equations:[26]

$$CO_2(g) \leftrightarrow CO_2(aq); \quad \text{(Equation 1)}$$

$$CO_2(aq) + H_2O \leftrightarrow H^+ + HCO_{3^-}; \quad \text{(Equation 2)}$$

$$HCO_{3^-} \leftrightarrow H^+ + CO_{3^{2-}}; \quad \text{(Equation 3)}$$

$$H_2O \leftrightarrow H^+ + OH^- \quad \text{(Equation 4)}$$

In 0.1 M $KHCO_3$, the alkalinity is balanced by acidity by the following equation:

$$[HCO_{3^-}] + 2[CO_{3^{2-}}] + [OH^-] = [K^+] + [H^+] \quad \text{(Equation 5)}$$

Typically, the aqueous CO_2 concentration decreases with increasing concentration of $KHCO_3$, a phenomenon known as the "salting-out effect."[27] However, the concentration of $KHCO_3$ used here, 0.1 M, allows the electrolyte to be treated as pure water for the purpose of equilibrium calculations, given that the CO_2 solubility is expected to be reduced by less than 5% (see Note S1). Knowing the equilibrium constants for Equations 1, 2, 3, and 4 at ambient temperature and pressure,[19] the aqueous CO_2 concentration was determined from the measured pH (see Figure S4 for the graph correlating pH with CO_2 concentration). The graph shows 0.1 M $KHCO_3$ saturated with CO_2 has a pH of 6.82 and corresponds to an aqueous CO_2 concentration of 34 mM. This was experimentally verified by equilibrating a 0.1 M $KHCO_3$ solution with 1 atm CO_2 gas (see Figure S5), thereby validating our assumption to treat 0.1 M $KHCO_3$ as pure water for equilibrium calculations.

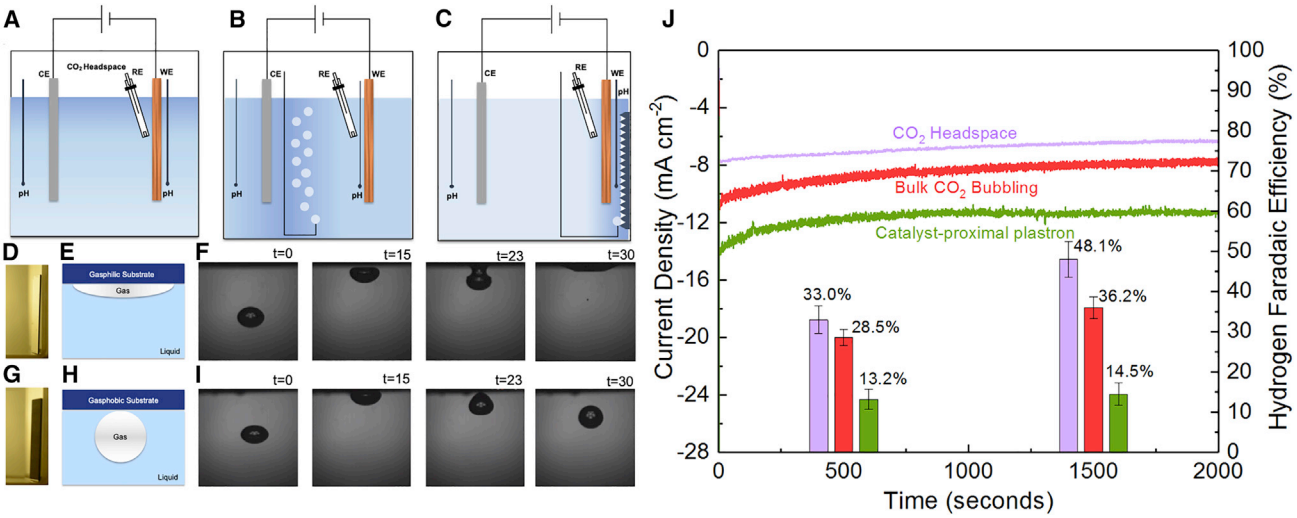

Figure 1. Catalyst-proximal plastron approach to enhance CO_2 electroreduction

(A) CO_2 headspace mode of CO_2 delivery.

(B) Bubbling CO_2 in the bulk.

(C) Catalyst-proximal CO_2 plastron layer on a gasphilic surface. The bubbling stream and plastron are held at the same approximate distance from the catalyst.

(D) A gasphilic silicon surface, which appears silvery due to an embedded plastron gas layer.

(E) Schematic of a gasphilic substrate that captures bubbles.

(F) Sequential high-speed camera images showing CO_2 bubble capture on a gasphilic surface (time shown in ms).

(G) A gasphobic silicon surface, which appears dark black.

(H) Schematic of a gasphobic substrate that does not capture bubbles.

(I) Sequential high-speed camera images showing CO_2 bubble bouncing on a gasphobic surface (time shown in ms). See Video S2.

(J) Comparison of CO_2 reduction current densities using the three delivery approaches shown in (A)–(C) along with the hydrogen Faradaic efficiency as a function of time (potential of -1.1 V_{RHE}). The error bars show the standard deviation obtained from three replicate runs. The reported current density is the geometric density and has been determined by dividing the measured current by the surface area of the wire (modeled as a cylinder).

As shown in Figures 1A–1C, two sensitive pH probes measured pH at two locations: in the CO_2-rich zone between the trap and the catalyst and in the bulk away from the catalyst (4 cm), from which the corresponding aqueous CO_2 concentration was determined. We found that, in the headspace mode of CO_2 delivery, although initially at the start of CO_2RR, the pH close to the catalyst indicated saturated conditions (pH ~6.82), it rapidly increased with reaction time, attributable to a decrease in the local CO_2 concentration due to fast consumption and sluggish replenishment of CO_2 as seen in Figure 2A. Both the pH probes (close and far) showed a similar increase in pH with time, given that the electrolyte was stirred constantly. In the bubbling case, even though the stream of bubbles was introduced at the same distance from the catalyst as the plastron, the pH increased during the reaction, showing that even the bubbling approach was not able to maintain a constant CO_2 concentration close to the catalyst. In contrast, not only did the plastron maintain a constant pH (and therefore local aqueous CO_2 concentration) near the catalyst throughout CO_2RR but also provided a richer, supersaturated concentration of CO_2, as confirmed by the local pH measurement (pH ~6.65) in Figure 2A.

In order to further confirm the enriched aqueous CO_2 concentration near the catalyst-proximal plastron, we used a colorimetric technique with the pH indicator bromothymol blue, which has a visual transition range between pH 5.2 and 7.4,[28] thereby being ideal for this study, considering that CO_2 saturation in the CO_2RR electrolyte occurs close to a pH of 6.8. We introduced drops of 0.05% bromothymol blue in a near-saturated electrolyte at two opposite ends in the cell and allowed the

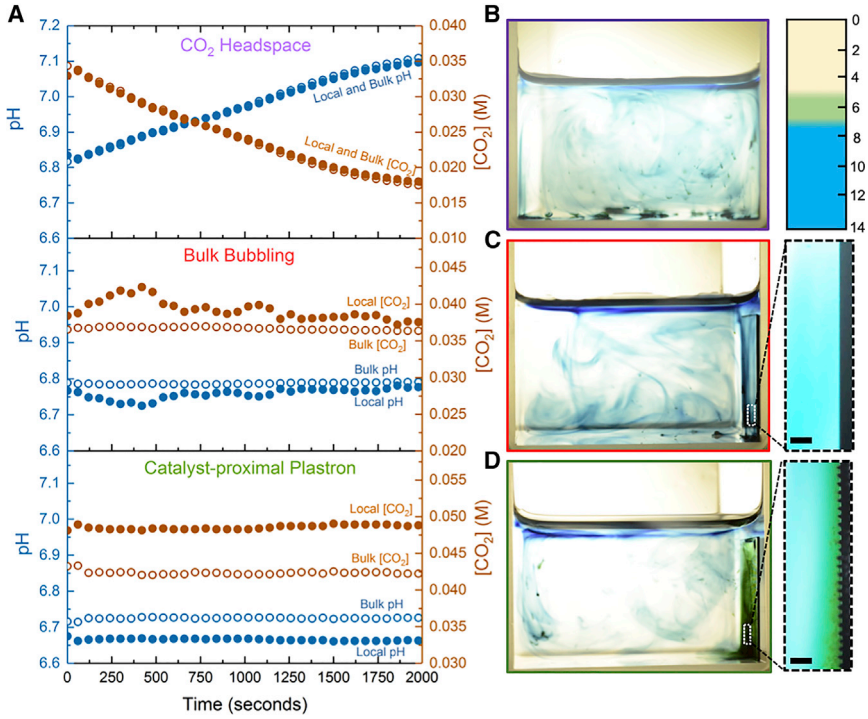

Figure 2. Characterization of CO_2 concentration in the electrolyte both close to the catalyst and further away from the catalyst

(A) pH measurements (blue circles) made during the CO_2RR experiment shown in Figure 1J for the headspace, bubbling, and plastron cases and the corresponding calculated CO_2 concentration (brown circles). Dark circles indicate measurements made close to the catalyst (~2 mm), and hollow circles indicate measurements made ~4 cm from the catalyst.

(B) Bromothymol blue added to a saturated 0.1M $KHCO_3$ with an ambient CO_2 headspace above it. It appears bluish at saturated conditions (see pH scale).

(C) Color evolution in a solution that has been recently bubbled with CO_2 with a magnified optical microscope image zooming in on a gasphobic silicon surface showing blue throughout.

(D) Color evolution in a solution with a gasphilic trap showing the CO_2 concentration difference (green indicating richer CO_2 concentration close to the trap relative to the bulk, which is blue). Optical microscope magnification reveals a green layer close to the trap emanating from the trapped gas within the textures. Scale bar shown in black represents 100 μm.

indicator to equilibrate for 2 min. As shown in Figure 2B, in the headspace approach, the solution remained blue throughout the electrolyte, indicating no gradients in CO_2 concentration. Similarly, when a stream of CO_2 bubbles was bubbled on a gasphobic silicon substrate, as shown in Figure 2C for 20 s, the electrolyte next to the substrate appeared blue as the rest of the electrolyte, showing no immediate benefit of the bubbling approach toward enhancing local CO_2 concentration, given the small residence time of the bubbles in the electrolyte (~1 s per bubble). However, when the same stream of bubbles was allowed to trap on the gasphilic surface and maintain a plastron layer, the solution close to the plastron instantly appeared green in sharp visual contrast to the rest of the blue solution as seen in Figure 2D, indicating a richer aqueous CO_2 concentration in the immediate vicinity of the plastron (see Video S3). In fact, after zooming in to the gasphilic surface using optical microscopy, we found that the enhanced CO_2 concentration emanates from the plastron contained within the textures of the gasphilic surface, as visualized by the thin green layer in the expanded image in Figure 2D. As long as the plastron layer is continuously replenished, CO_2 supersaturation is maintained throughout the CO_2RR experiment, as shown by the pH measurements in Figure 2A.

To investigate the mass transfer advantage of the plastron versus bubbling approaches, we experimentally visualized the concentration evolution of the two approaches using bromothymol blue, which was introduced at two opposite ends of the cell while the CO_2 was continuously flowing (see Videos S4 and S5). The bubbling stream induced mixing as visualized by the eddies, and the CO_2 transferred from the bubbles to the electrolyte was rapidly convected away into the bulk, as shown by the blue color (see the dashed rectangle showing extent of convection in Figure S6). In contrast, the color close to the plastron remained green, indicating that high CO_2 concentration is maintained local to the plastron without being convected away and diluted into the bulk electrolyte as with the bubbling approach. Despite the bubbling stream and the plastron being at the same distance from the catalyst, the steady-state CO_2RR current density using the plastron approach was 33% greater than the plastron approach, and the H_2 Faradaic efficiency was over two times lower, as shown in Figure 1. By increasing the gas-liquid interfacial area and the residence time in the system, the CO_2-electrolyte mass transfer was enhanced using the plastron, and a high local concentration of CO_2 was maintained throughout the CO_2RR reaction, which drives CO_2 to the catalyst surface and maintains CO_2RR performance. By operating at atmospheric pressure, this approach has an inherent advantage over pressurized reactors by achieving high localized CO_2 concentrations and mass transfer rates that maintain CO_2RR performance.

Enhancement of C2+ products

We performed equivalent experiments in a standard CO_2RR H-cell connected to a gas chromatograph (GC) in order to characterize the effect of the catalyst-proximal plastron on the product distribution (see Experimental Methods). As seen in Figure 3E, using smooth copper (SEM images in Figures 3A and 3B), the plastron approach resulted in the lowest H_2 Faradaic efficiency as compared to other delivery approaches at -1.1 V_{RHE}, reducing from 33% in the headspace approach to 13%. At the same time, the ethylene Faradaic efficiency was also enhanced from 2% to 18%, indicating a significant increase in a valuable C2 product as well as enhancement in formate from 10% to 25%. It is clear that these changes in product distribution result directly from enhancement in local aqueous CO_2 concentration, as shown by squares in Figure 3C.

We synthesized nanostructured copper using the thermal treatment technique previously described in literature (see Experimental Procedures and SEM images in Figures 3D and 3E).[12] Porous, nanostructured copper is an attractive catalyst, as it has been shown to generate more C2 and C3 products especially at low overpotentials (>-1.0 V_{RHE}), as compared to polycrystalline copper.[12,23,29] However, at potentials more negative than -1.0 V_{RHE}, mass transport limitations are reached, due to which the catalyst evolves primarily hydrogen, as the CO_2 that is rapidly consumed from the vicinity of the catalyst is not adequately replenished.[21-23] Indeed, as shown in Figure 3F, we observe that, at -1.1 V_{RHE}, both the headspace and bubbling approaches result in an over 50% Faradaic efficiency for hydrogen, which is consistent with observations from previous studies at similar potentials on oxide-derived copper (see Table S1 for a comprehensive comparison).[23,30-32] With a catalyst-proximal plastron, similar to the smooth polycrystalline case, the local CO_2 available to the catalyst is enhanced and replenished quickly, thereby leading to a dramatic decrease in the H_2 Faradaic efficiency from 62% to 33% and an increased production of valuable C2+ products, such as ethanol, ethane, ethylene, acetone, acetate, and propanol. The local CO_2 concentrations follow a similar trend as in the case of the smooth copper, with the catalyst-proximal plastron showing the highest local CO_2 concentration. In addition, the CO_2RR-specific current density is also enhanced relative to the headspace approach, similar to observations on smooth copper (see Table S1).

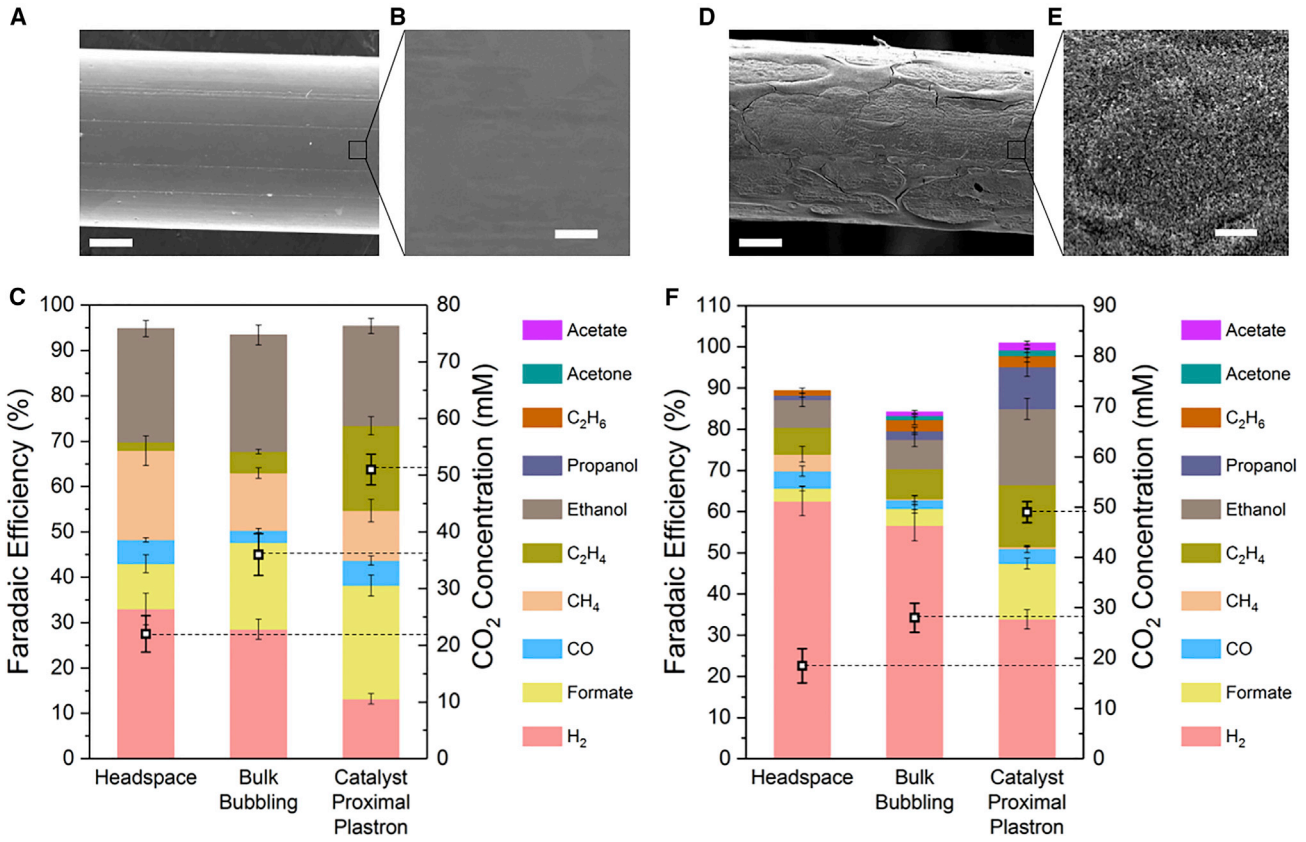

Figure 3. Faradaic efficiencies obtained from the catalyst-proximal plastron approach on copper

(A) SEM image showing a polycrystalline electropolished Cu wire (scale bar represents 100 μm).

(B) Zoomed inset of (A)—scale bar represents 1 μm.

(C) Comparison of product distribution and the corresponding aqueous CO_2 concentration for smooth copper. Error bars for Faradaic efficiencies of all products are included in the individual bar graphs, as well as error bars for the aqueous CO_2 concentration, as represented by the squares. The error bars show standard deviations from three replicate runs. All experiments are at −1.1 V_{RHE} in 0.1 M $KHCO_3$ saturated with CO_2.

(D) SEM image showing an oxide-derived nanostructured Cu wire (scale bar represents 100 μm).

(E) Zoomed inset of (D) showing nanotextures—scale bar represents 1 μm.

(F) Comparison of product distribution and the corresponding CO_2 concentration for nanostructured copper. Error bars for Faradaic efficiencies of all products are included in the individual bar graphs, as well as error bars for the aqueous CO_2 concentration, as represented by the squares. The error bars show standard deviations from three replicate runs. All experiments are at −1.1 V_{RHE} in 0.1 M $KHCO_3$ saturated with CO_2.

The coupling of C2+ products requires the arrival and adsorption of several CO_2 molecules to the surface throughout the CO_2RR reaction.[33,34] Using the gasphilic trap, not only is the CO_2 concentration enhanced close to the catalyst, as seen Figure 2, but this enhanced concentration is held proximal to the catalyst, as visualized in Figure S6 and Videos S3 and S4, thereby enabling the arrival and adsorption of CO_2 molecules to the catalyst surface and promoting formation of attractive C2+ products. The total Faradaic efficiency for C2+ products is increased from 21% to 49% on nanotextured copper and from 30% to 40% on smooth copper by changing from the bubbling approach to the catalyst-proximal plastron approach, consistent with our previous hypothesis of enhanced mass transport and CO_2 concentration.

Comparison with other recent CO_2RR studies using copper

Figure 4 compares the results from the present study using the catalyst-proximal plastron approach with other relevant CO_2RR studies on copper. Comparing with seven different CO_2RR studies that were conducted on smooth, polycrystalline copper at approximately the same potential and electrolyte concentration, the

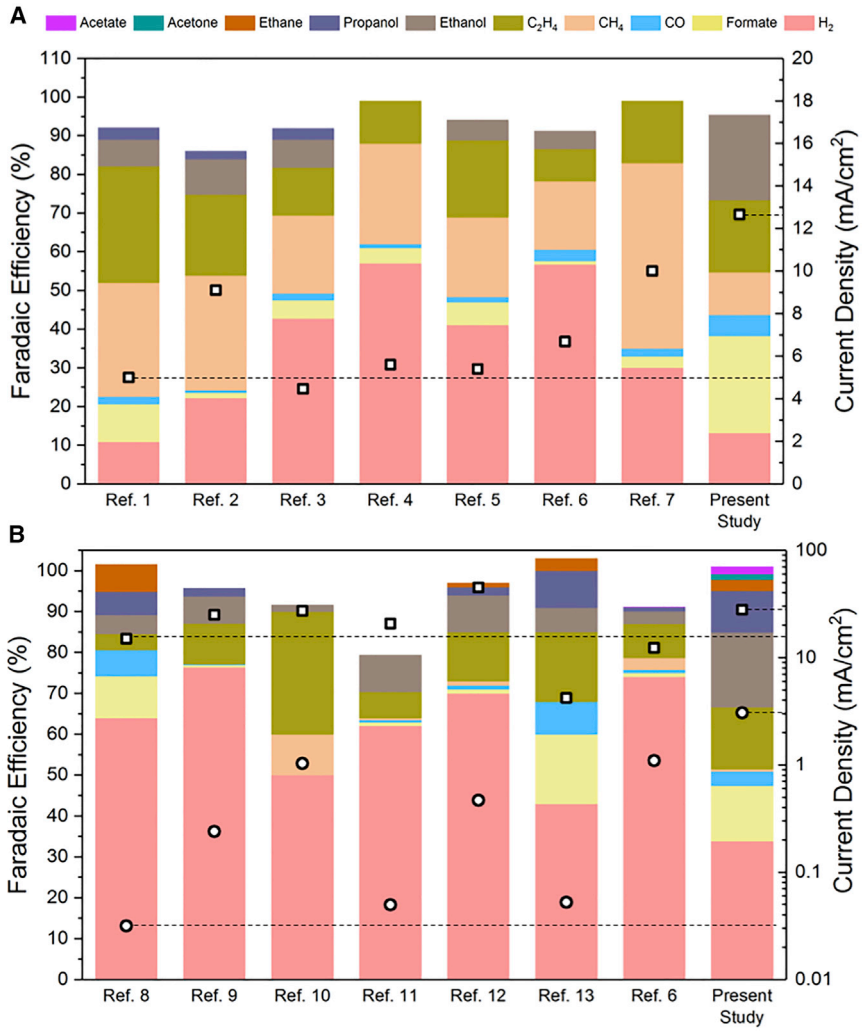

Figure 4. Comparison with recent aqueous-phase CO_2RR studies

(A) Product distribution and geometric current density (shown by square symbols) from the present study using the catalyst-proximal plastron approach as compared to seven different reported studies on polycrystalline copper at potentials equal to or similar to −1.1 V_{RHE} in 0.1M $KHCO_3$: Ref. 1;[9] Ref. 2;[4] Ref. 3;[35] Ref. 4;[36] Ref. 5;[37] Ref. 6;[32] and Ref. 7.[38] The reported current density is the geometric density and has been determined by dividing the measured current by the surface area of the wire (modeled as a cylinder).

(B) Product distribution and geometric current density (shown by square symbols) as well as ECSA-normalized current density (shown by circles) from the present study using the catalyst-proximal plastron approach as compared to seven different reported studies on nanostructured copper: Ref. 8;[12] Ref. 9;[23] Ref. 10;[13] Ref. 11;[30] Ref. 12;[31] and Ref. 13.[39] See Table S1 for detailed comparison and description of the catalysts used by each reference.

catalyst-proximal plastron approach reports the highest current density together with highest formate (~25%) and ethanol (~22%) Faradaic efficiencies, as shown in Figure 4A.[4,9,32,35-38] Although our reported H_2 Faradaic efficiency (~13%) is slightly greater than the seminal work of Hori et al.[9] on copper (~10%), we report a greater overall current density as well as CO_2RR-specific current density, as shown in Table S1. We also show the lowest H_2 Faradaic efficiency when compared to more recent studies on polycrystalline copper performed within the last decade at −1.1 V_{RHE}.[4,32,35-38]

Similarly, when compared to previous CO_2RR studies using nanotextured copper, as shown in Figure 4B, the catalyst-proximal plastron approach results in the lowest H_2 Faradaic efficiency and the highest ethanol, n-propanol, acetone, and acetate Faradaic efficiencies determined at −1.1 V_{RHE}. In fact, to our knowledge, our study is the first to report acetone and acetate at Faradaic efficiencies exceeding 1%. Although there are large variances in the geometric current densities on nanostructured copper between different studies as shown by the square symbols in Figure 4B, our study reports the highest current density when normalized by the electrochemically active surface area (ECSA), as shown by the circles in Figure 4B (see Experimental Procedures and Figure S10 for details on the ECSA determination). Recent literature on CO_2RR has highlighted the importance of normalizing the current density with respect to ECSA on nanotextured catalysts in order to truly ascertain improvements in intrinsic CO_2RR activity against comparable catalysts,[22,40] and thus, the effect of the catalyst-proximal plastron can be further highlighted on nanostructured copper due to enhanced local CO_2 concentration.

Figure 4B also shows that nanotextured copper has a lower overall current density than smooth, polycrystalline copper in Figure 4A when normalized by ECSA, despite having similar local CO_2 concentration using the catalyst-proximal plastron approach, as seen in Figure 3. Comparing the headspace, bubbling, and catalyst-proximal plastron approaches, we find that the HER current is progressively suppressed on nanotextured copper (see Table S1; HER current obtained by multiplying H_2 Faradaic efficiency by the total current density), a trend that is similarly reflected by polycrystalline copper as well. However, because the HER current observed on nanotextured copper is similar in magnitude to that of polycrystalline copper, the plastron approach is not mass transport limited, despite having a lower overall current density. We believe that the lower ESCA-normalized CO_2RR current density on oxide-derived copper (when compared to smooth, polycrystalline copper) can be attributed to catalyst-level defects on the oxide-derived copper, such as undercoordinated sites, readsorption of reaction products, preferential faceting, and grain boundaries,[13,22,41] rather than mass-transport limitations arising from the locally available CO_2. Hence, the catalyst-proximal plastron approach can truly deconvolute mass-transport effects and inherent catalyst defects in nanostructured copper, especially at potentials more negative than −1.0 V_{RHE}. As shown in Table S1, no matter whether the catalyst is smooth or nanostructured, the catalyst-proximal plastron increases the intrinsic CO_2RR current density while minimizing hydrogen co-evolution when compared with other CO_2RR studies on state-of-the-art catalysts.[12,13,23,30-32,39] Thus, the catalyst-proximal plastron approach can truly reveal the attractive capabilities of nanostructured copper, which have been typically obfuscated by hydrogen co-evolution.

DISCUSSION

We note here that gas diffusion electrodes (GDEs) have evolved over the years to overcome CO_2 mass transport limitations and deliver high current densities and Faradaic efficiencies for C2+ products in a continuous flow configuration.[17,42-44] Although GDEs have been recognized as the practical, scalable path forward for CO_2 electroconversion,[18,22] GDEs have a complicated interface that combine multiple elements, including hydrophobicity, and it is not straightforward to elucidate intrinsic catalytic performance using GDEs, as kinetics and transport are coupled. Therefore, many fundamental CO_2RR studies are performed in aqueous-phase electrolytic cells (such as H-cells).[18,45] Such aqueous-phase systems, however, have been hitherto mass transport limited, as the CO_2 that is depleted from the reaction is not

rapidly replenished, which has made it difficult to assess CO_2RR performance against gas diffusion systems.[18,45] The plastron approach can bridge the gap between GDEs and aqueous-phase systems by overcoming the mass transport limitations of aqueous systems. For example, the reported Faradaic efficiencies for C2+ alcohols (ethanol and propanol) on nanotextured copper for aqueous-phase systems as reported in Figure 4B show <15% total Faradaic efficiency for C2+ alcohols at the same applied potential when compared to GDE systems. By using the catalyst-proximal plastron approach, we observe a Faradaic efficiency of 30% for C2+ alcohols, as shown in Figure 3F, which is similar to the highest reported Faradaic efficiency of 32% using copper in a GDE.[34] Therefore, by overcoming mass transport limitations in a simple aqueous-phase system, the plastron approach can provide target CO_2RR Faradaic efficiencies that can inform the selection and incorporation of catalysts toward enabling optimum GDE performance. Future studies can evaluate specific high-surface area catalyst architectures typically used in GDEs along with catalyst-proximal plastron to obtain catalyst activity and selectivity in aqueous-phase systems.

In addition, theoretical studies can be performed in the future to predict the specific pH conditions and chemical composition at the electrode surface.

In summary, we show that, by maintaining a CO_2 plastron layer on a gasphilic surface in close proximity to a smooth, electropolished copper catalyst, the intrinsic current density associated with CO_2RR is increased by close to two times as compared to conventional absorption from a CO_2 headspace. Furthermore, the CO_2RR current density does not deteriorate with time, and this is directly due to the enhanced local CO_2 concentration available to the catalyst that is sustained throughout the reaction and the improved gas-liquid mass transfer using the plastron. Consequently, the Faradaic efficiency associated with hydrogen is reduced to as low as 13% at −1.1 V_{RHE}, and when compared to previous studies at the same potentials, we report the lowest hydrogen Faradaic efficiency combined with the highest CO_2RR current density on a smooth, electropolished copper surface. H_2 Faradaic efficiency is suppressed from 62% to 33% on oxide-derived nanostructured copper, along with the generation of attractive C2+ products, including ethylene, ethanol, and n-propanol, as well as acetone and acetate at enhanced concentrations. We believe that this transformational approach can truly elucidate the attractive capabilities of both smooth and nanostructured copper, which have been typically hindered by hydrogen co-evolution, as well as combined with many catalyst-side advances in CO_2RR to further enhance activity and selectivity.

EXPERIMENTAL PROCEDURES

Resource availability

Lead contact

Further information and requests for resources should be directed to the lead contact, Kripa K. Varanasi (varanasi@mit.edu).

Materials availability

This study did not generate any unique materials.

Data and code availability

This study did not generate code. All of the data associated with this study are represented in the manuscript and Supplemental Information. Other data are available from the lead contact upon reasonable request.

Preparation of electropolished copper

Copper wire (99.999% purity; 0.5 mm in diameter) was obtained from Goodfellow Corporation. Prior to electrochemical experiments, the wire was rubbed by sandpaper followed by sonicating in deionized (DI) water and subsequent electropolishing in 85% H_3PO_4 (Sigma Aldrich; 85 wt % in H_2O; 99.99% trace metals basis) for 1 min at 3 V and 10 min at :1.5–2 V (based on the oxidation peak from a cyclic voltammetry measurement) versus a graphite counter electrode. The wire was then thoroughly rinsed and sonicated in DI water and was immediately used for electrochemical experiments. The geometric surface area of the catalyst was determined by measuring the wire diameter and length (modeling the wire as a cylinder), and the surface roughness was assumed to be unity, similar to previous studies. The geometric current density was determined by dividing the measured current by this calculated surface area.

Preparation of oxide-derived nanostructured copper

Oxide-derived nanostructured copper (OD-Cu) was synthesized using the techniques published previously.[12] The electropolished Cu wire described above was heated to 500°C at a rate of 10°C/min and maintained at 500°C for 1 h, after which it was cooled down slowly over a period of 12 h. The sample was then electrochemically reduced to copper during the first 5 min of the CO_2RR reaction. The diameter of the wire was determined from the SEM image shown in Figure 3, and the geometric surface area was calculated by modeling the wire as a cylinder. The geometric current density was then determined by dividing the measured current by the surface area of the wire.

Preparation of gasphilic traps

The gasphilic surfaces (1″ by 1″) to develop plastrons were fabricated on silicon using a 1,064 nm laser (TYMKA Electrox), which created a series of closely packed pyramidal textured features spaced approximately 50 μm apart and 50 μm deep. The features also had nanotexture atop the pyramids, which was naturally formed from the ablating silicon. The samples were then cleaned in an oxygen plasma chamber (PDC-32G-2 by Harrick Plasma) at 200 mTorr for 10 min followed by chemical vapor deposition using fluorosilane to render them hydrophobic and, consequently, gasphilic.

Electrochemistry experiments

The CO_2RR experiments described in Figures 1 and 2 were performed in a custom-made clean cubical glass cell measuring 5 cm by 5 cm by 5 cm. Due to the flat walls of the glass cell, it was possible to visualize the catalyst and the gasphilic trap during the reaction (see Figures S1 and S2). The cubical geometry of the cell also made it possible to insert electrodes and pH probes at precise distances from one another. A coiled platinum wire (99.99% purity; Pine Research) was used as the counter electrode, which was isolated from the main electrolyte by storing in a fritted glass tube. In order to minimize metal contamination that can impact CO_2RR performance, all glassware was cleaned in sequence by 1 M KOH (Alfa Aesar; 99.99%), Aqua Regia (3:1 HCl:HNO_3), and boiling DI water (Millipore; 18.2 M Ω cm) for 1 h each. 0.1 M $KHCO_3$ electrolyte was prepared by vigorously bubbling a solution of 0.1 M KOH (Millipore Suprapur; >99.995%) in DI water (Millipore; 18.2 M Ω cm) with CO_2 gas (Airgas; 99.999% purity) for at least 1 h. The pH of the electrolyte was confirmed to be 6.8 prior to use in CO_2RR. In fact, in the catalyst-proximal plastron approach, the CO_2 was bubbled directly on the gasphilic trap along with the bulk, thereby resulting in a pH <6.8 prior to the experiment. In the CO_2 headspace approach, the electrolyte was constantly stirred by a stir bar, thereby ensuring it was well mixed.

All chronoamperometry experiments were conducted at −1.1 V_{RHE} using an Ag/AgCl leak-free reference electrode (Pine Research) calibrated to the reference hydrogen electrode (RHE), and iR correction was applied post-electrolysis. pH effects were taken into consideration while calculating the electrode potentials from RHE using the following equation:

$$E_{RHE} = E_{Ag/AgCl} + 0.197 + 0.0591pH$$

The current densities reported in Figure 4 and Table S1 represent averages of at least three measurements. Local pH measurements were made using the 9810n series probe from Fisher Scientific (~1 mm diameter), although the bulk pH was measured using a 3-mm-diameter probe from Hanna Instruments. The aqueous CO_2 concentration reported in Figure 3 was determined from the pH measured 10 min into CO_2RR and represents an average of three measurements. Figure S7 shows the impact of changing the distance between the plastron and the catalyst on the CO_2RR current density. It is advantageous to perform CO_2RR as proximal to the catalyst as possible.

Determining Faradaic efficiencies

For the equivalent experiments requiring characterization of product distribution, CO_2RR was performed in a two-compartment H-cell, with a Pt mesh counter electrode separated from the catholyte by a Nafion 117 membrane (obtained from the Fuel Cell Store). The same cleaning procedures described earlier were used with all glassware, and the Nafion 117 membrane was conditioned prior to electrochemical measurements sequentially by 0.5 M H_2SO_4, 0.5 M H_2O_2, and 0.5 M $KClO_4$ for ~1 h each and then rinsed with DI water prior to electrochemical measurements. The catalyst-proximal plastron was developed on the gasphilic trap and kept at the exact same distance from the catalyst as in the cubical cell described previously. Product detection of gas-phase products were made by gas chromatography (SRI Instruments; 6'' Hayesep-D and 6'' Molsieve-13× columns), in which the headspace of the catholyte compartment was continuously flushed with CO_2 into the GC sample loop. H_2 was detected by the thermal conductivity detector (TCD) although organic compounds (CH_4, CO, C_2H_4, and C_2H_6) were detected by flame ionization detector (FID). The first gas sampling was taken 10 min into the chronoamperometry measurement, and the second was taken 30 min into the measurement. Liquid-phase products were analyzed after electrolysis using nuclear magnetic resonance (NMR), specifically ^{1}H-NMR (Bruker 500 MHz). For this procedure, 35 μL of a 100 mM phenol and 100 mM dimethyl sulfoxide (DMSO) reference solution in D_2O standard was added to 700 μL of collected electrolyte, and a water-suppression protocol was followed to minimize the water peak intensity. Figure S8 shows the effect of potential on CO_2RR current densities and Faradaic efficiencies. Although both −1.1 V_{RHE} and −1.0 V_{RHE} potentials show improvement in CO_2RR performance by using the plastron, −1.1 V_{RHE} is optimal to show the most significant impact of the plastron approach.

X-ray photoelectron spectroscopy (XPS) characterization

XPS surface analysis was performed on the electropolished copper catalyst both before and after CO_2RR (PHI Versaprobe II series XPS). Survey spectra of the catalyst sample used in the catalyst-proximal plastron approach are shown in Figure S9. No metallic contaminants were detected both before and after CO_2RR; the K, O, and C peaks on the post-electrolysis catalyst sample can be attributed to trace electrolyte salts left on the catalyst surface.

Determination of ECSA

The ECSA of the nanostructured oxide-derived copper catalyst was determined using the double-layer capacitance method as described previously in literature.[12]

Using 0.1M $HClO_4$ as the electrolyte, cyclic voltammetry scans were conducted in a potential range where Faradaic processes are absent (see Figure S10) at five different scan rates from 20 mV/s to 100 mV/s. The current density was then plotted against the scan rate, which resulted in an approximately linear graph, from which the slope was determined and the double-layer capacitance was calculated. The corresponding roughness factor (see Table S2) was calculated by dividing the capacitance of the nanostructured catalyst by that of the smooth, electropolished catalyst (roughness assumed to be 1). The roughness factor was then multiplied by the geometric area in all ECSA-normalized current density calculations.

Assembly of catalyst-proximal plastrons

To demonstrate that the enhancement in the CO_2RR current density by using the catalyst-proximal plastron approach is replicable even in catalyst systems that have an increased area, we fabricated a simple device that consists of five electropolished copper catalyst wires placed in close proximity to their respective plastrons, as shown in Figure S11A and S11B below using the same volume of 0.1 M $KHCO_3$ as our previous experiment in Figure 1 in the manuscript. For comparison, a similar configuration of catalysts with the same surface area was made where instead CO_2 was bubbled in the bulk electrolyte close to the catalyst at the same flowrate as shown in Figures S11C and S11D. It is evident from Figure S11E that the CO_2RR current is enhanced simply by introducing the bubbles on traps close to the catalyst than in bulk for the same flow rate and catalyst surface area. In fact, the ratio of the measured currents at steady state between the plastron and bubbling approaches is consistent with the ratio of current densities measured previously with a single catalyst seen in Figure 1J. Furthermore, the local CO_2 concentration (as determined by measuring pH) is enhanced and maintained in the catalyst-proximal plastron approach. Each catalyst-proximal plastron provides greater mass transfer of CO_2 relative to the bubbling approach, thereby maintaining the local CO_2 concentration as well as the CO_2RR current. Each individual catalyst in the assembly benefits from the supersaturated CO_2 concentration emanating from within the plastrons, as visualized in Figure 2D. Even when the catalyst area is increased for the same volume of electrolyte (thereby drawing a greater current and consuming more CO_2 in the same electrolyte volume), the catalyst-proximal plastron approach is able to enhance and maintain CO_2RR performance relative to the bubbling approach.

SUPPLEMENTAL INFORMATION

Supplemental Information can be found online at https://doi.org/10.1016/j.xcrp.2020.100318.

ACKNOWLEDGMENTS

This work was supported by Eni S.p.A through the MIT Energy Initiative. S.K. acknowledges support from the NSERC Postgraduate Award.

AUTHOR CONTRIBUTIONS

The manuscript was written through contributions of all authors. K.K.V. and Y.-S.H. conceptualized the research and supervised the project. S.K. and J.H. performed the research. S.K. fabricated textured gasphilic samples and performed chronoamperometry, pH, and colorimetry measurements. J.H. and S.K. performed the GC and NMR measurements. All authors discussed the results and analyzed the data. S.K. and K.K.V. wrote the manuscript, and others commented on and edited the manuscript.

DECLARATION OF INTERESTS

Y.S.H. is a board member at *Cell Reports Physical Science*.

Received: September 1, 2020
Revised: December 7, 2020
Accepted: December 17, 2020
Published: January 25, 2021

REFERENCES

1. Snoeckx, R., and Bogaerts, A. (2017). Plasma technology - a novel solution for CO_2 conversion? Chem. Soc. Rev. *46*, 5805–5863.

2. De Luna, P., Hahn, C., Higgins, D., Jaffer, S.A., Jaramillo, T.F., and Sargent, E.H. (2019). What would it take for renewably powered electrosynthesis to displace petrochemical processes? Science *364*, eaav3506.

3. Vayenas, C.G., White, R.E., and Gamboa-Aldeco, M.E. (2008). Modern Aspects of Electrochemistry 42 (Springer Science & Business Media).

4. Kuhl, K.P., Cave, E.R., Abram, D.N., and Jaramillo, T.F. (2012). New insights into the electrochemical reduction of carbon dioxide on metallic copper surfaces. Energy Environ. Sci. *5*, 7050–7059.

5. Qiao, J., Liu, Y., Hong, F., and Zhang, J. (2014). A review of catalysts for the electroreduction of carbon dioxide to produce low-carbon fuels. Chem. Soc. Rev. *43*, 631–675.

6. Li, J., Chen, G., Zhu, Y., Liang, Z., Pei, A., Wu, C.-L., Wang, H., Lee, H.R., Liu, K., Chu, S., et al. (2018). Efficient electrocatalytic CO_2 reduction on a three-phase interface. Nat. Catal. *1*, 592–600.

7. Leonard, M.E., Clarke, L.E., Forner-Cuenca, A., Brown, S.M., and Brushett, F.R. (2020). Investigating electrode flooding in a flowing electrolyte, gas-fed carbon dioxide electrolyzer. ChemSusChem *13*, 400–411.

8. Sebastián-Pascual, P., Mezzavilla, S., Stephens, I.E.L., and Escudero-Escribano, M. (2019). Structure-sensitivity and electrolyte effects in CO_2 electroreduction: from model studies to applications. ChemCatChem *11*, 3626–3645.

9. Hori, Y., Murata, A., and Takahashi, R. (1989). Formation of hydrocarbons in the electrochemical reduction of carbon dioxide at a copper electrode in aqueous solution. J. Chem. Soc., Faraday Trans. I *85*, 2309–2326.

10. De Luna, P., Quintero-Bermudez, R., Dinh, C.-T., Ross, M.B., Bushuyev, O.S., Todorović, P., Regier, T., Kelley, S.O., Yang, P., and Sargent, E.H. (2018). Catalyst electro-redeposition controls morphology and oxidation state for selective carbon dioxide reduction. Nat. Catal. *1*, 103–110.

11. Kas, R., Kortlever, R., Yılmaz, H., Koper, M.T.M., and Mul, G. (2015). Manipulating the hydrocarbon selectivity of copper nanoparticles in CO_2 electroreduction by process conditions. ChemElectroChem *2*, 354–358.

12. Li, C.W., and Kanan, M.W. (2012). CO2 reduction at low overpotential on Cu electrodes resulting from the reduction of thick Cu2O films. J. Am. Chem. Soc. *134*, 7231–7234.

13. Mistry, H., Varela, A.S., Bonifacio, C.S., Zegkinoglou, I., Sinev, I., Choi, Y.-W., Kisslinger, K., Stach, E.A., Yang, J.C., Strasser, P., and Cuenya, B.R. (2016). Highly selective plasma-activated copper catalysts for carbon dioxide reduction to ethylene. Nat. Commun. *7*, 12123.

14. Kim, Y.-G., Baricuatro, J.H., Javier, A., Gregoire, J.M., and Soriaga, M.P. (2014). The evolution of the polycrystalline copper surface, first to Cu(111) and then to Cu(100), at a fixed CO_2RR potential: a study by operando EC-STM. Langmuir *30*, 15053–15056.

15. Hahn, C., Hatsukade, T., Kim, Y.-G., Vailionis, A., Baricuatro, J.H., Higgins, D.C., Nitopi, S.A., Soriaga, M.P., and Jaramillo, T.F. (2017). Engineering Cu surfaces for the electrocatalytic conversion of CO_2: Controlling selectivity toward oxygenates and hydrocarbons. Proc. Natl. Acad. Sci. USA *114*, 5918–5923.

16. Wu, Y.A., McNulty, I., Liu, C., Lau, K.C., Liu, Q., Paulikas, A.P., Sun, C.-J., Cai, Z., Guest, J.R., Ren, Y., et al. (2019). Facet-dependent active sites of a single Cu_2O particle photocatalyst for CO_2 reduction to methanol. Nat. Energy *4*, 957–968.

17. Dinh, C.-T., Burdyny, T., Kibria, M.G., Seifitokaldani, A., Gabardo, C.M., García de Arquer, F.P., Kiani, A., Edwards, J.P., De Luna, P., Bushuyev, O.S., et al. (2018). CO_2 electroreduction to ethylene via hydroxide-mediated copper catalysis at an abrupt interface. Science *360*, 783–787.

18. Burdyny, T., and Smith, W.A. (2019). CO_2 reduction on gas-diffusion electrodes and why catalytic performance must be assessed at commercially-relevant conditions. Energy Environ. Sci. *12*, 1442–1453.

19. Elhajj, J., Al-Hindi, M., and Azizi, F. (2014). A review of the absorption and desorption processes of carbon dioxide in water systems. Ind. Eng. Chem. Res. *53*, 2–22.

20. Lobaccaro, P., Singh, M.R., Clark, E.L., Kwon, Y., Bell, A.T., and Ager, J.W. (2016). Effects of temperature and gas-liquid mass transfer on the operation of small electrochemical cells for the quantitative evaluation of CO_2 reduction electrocatalysts. Phys. Chem. Chem. Phys. *18*, 26777–26785.

21. Ren, D., Fong, J., and Yeo, B.S. (2018). The effects of currents and potentials on the selectivities of copper toward carbon dioxide electroreduction. Nat. Commun. *9*, 925.

22. Nitopi, S., Bertheussen, E., Scott, S.B., Liu, X., Engstfeld, A.K., Horch, S., Seger, B., Stephens, I.E.L., Chan, K., Hahn, C., et al. (2019). Progress and perspectives of electrochemical CO_2 reduction on copper in aqueous electrolyte. Chem. Rev. *119*, 7610–7672.

23. Lum, Y., Yue, B., Lobaccaro, P., Bell, A.T., and Ager, J.W. (2017). Optimizing C–C coupling on oxide-derived copper catalysts for electrochemical CO_2 reduction. J. Phys. Chem. C *121*, 14191–14203.

24. de Maleprade, H., Clanet, C., and Quéré, D. (2016). Spreading of bubbles after contacting the lower side of an aerophilic slide immersed in water. Phys. Rev. Lett. *117*, 094501.

25. Panchanathan, D., Rajappan, A., Varanasi, K.K., and McKinley, G.H. (2018). Plastron regeneration on submerged superhydrophobic surfaces using in situ gas generation by chemical reaction. ACS Appl. Mater. Interfaces *10*, 33684–33692.

26. Gupta, N., Gattrell, M., and MacDougall, B. (2006). Calculation for the cathode surface concentrations in the electrochemical reduction of CO_2 in $KHCO_3$ solutions. J. Appl. Electrochem. *36*, 161–172.

27. Singh, M.R., Clark, E.L., and Bell, A.T. (2015). Effects of electrolyte, catalyst, and membrane composition and operating conditions on the performance of solar-driven electrochemical reduction of carbon dioxide. Phys. Chem. Chem. Phys. *17*, 18924–18936.

28. Davis, C.E., and Salisbury, H.M. (1929). Chart of indicators useful for pH measurements. Ind. Eng. Chem. Anal. Ed. *1*, 92.

29. Ren, D., Deng, Y., Handoko, A.D., Chen, C.S., Malkhandi, S., and Yeo, B.S. (2015). Selective electrochemical reduction of carbon dioxide to ethylene and ethanol on copper(I) oxide catalysts. ACS Catal. *5*, 2814–2821.

30. Raciti, D., Livi, K.J., and Wang, C. (2015). Highly dense Cu nanowires for low-overpotential CO2 reduction. Nano Lett. *15*, 6829–6835.

31. Handoko, A.D., Ong, C.W., Huang, Y., Lee, Z.G., Lin, L., Panetti, G.B., and Yeo, B.S. (2016). Mechanistic insights into the selective electroreduction of carbon dioxide to ethylene on Cu_2O-derived copper catalysts. J. Phys. Chem. C *120*, 20058–20067.

32. Kwon, Y., Lum, Y., Clark, E.L., Ager, J.W., and Bell, A.T. (2016). CO_2 electroreduction with enhanced ethylene and ethanol selectivity by nanostructuring polycrystalline copper. ChemElectroChem *3*, 1012–1019.

33. Bushuyev, O.S., De Luna, P., Dinh, C.T., Tao, L., Saur, G., van de Lagemaat, J., Kelley, S.O., and Sargent, E.H. (2018). What should we make with CO2 and how can we make it? Joule *2*, 825–832.

34. Fan, L., Xia, C., Yang, F., Wang, J., Wang, H., and Lu, Y. (2020). Strategies in catalysts and electrolyzer design for electrochemical CO_2 reduction toward C_{2+} products. Sci. Adv. *6*, eaay3111.

35. Han, Z., Kortlever, R., Chen, H.-Y., Peters, J.C., and Agapie, T. (2017). CO_2 reduction selective for $C_{\geq 2}$ products on polycrystalline copper with N-substituted pyridinium additives. ACS Cent. Sci. *3*, 853–859.

36. Chen, C.S., Handoko, A.D., Wan, J.H., Ma, L., Ren, D., and Yeo, B.S. (2015). Stable and selective electrochemical reduction of carbon dioxide to ethylene on copper mesocrystals. Catal. Sci. Technol. *5*, 161–168.

37. Loiudice, A., Lobaccaro, P., Kamali, E.A., Thao, T., Huang, B.H., Ager, J.W., and Buonsanti, R. (2016). Tailoring copper nanocrystals towards C2 products in electrochemical CO2 reduction. Angew. Chem. Int. Ed. Engl. *55*, 5789–5792.

38. Kimura, K.W., Fritz, K.E., Kim, J., Suntivich, J., Abruña, H.D., and Hanrath, T. (2018). Controlled selectivity of CO_2 reduction on copper by pulsing the electrochemical potential. ChemSusChem *11*, 1781–1786.

39. Ma, M., Djanashvili, K., and Smith, W.A. (2016). Controllable hydrocarbon formation from the electrochemical reduction of CO2 over Cu nanowire arrays. Angew. Chem. Int. Ed. Engl. *55*, 6680–6684.

40. Clark, E.L., Resasco, J., Landers, A., Lin, J., Chung, L.-T., Walton, A., Hahn, C., Jaramillo, T.F., and Bell, A.T. (2018). Standards and protocols for data acquisition and reporting for studies of the electrochemical reduction of carbon dioxide. ACS Catal. *8*, 6560–6570.

41. Lu, Q., Rosen, J., and Jiao, F. (2015). Nanostructured metallic electrocatalysts for carbon dioxide reduction. ChemCatChem *7*, 38–47.

42. Wang, Y., Shen, H., Livi, K.J.T., Raciti, D., Zong, H., Gregg, J., Onadeko, M., Wan, Y., Watson, A., and Wang, C. (2019). Copper nanocubes for CO_2 reduction in gas diffusion electrodes. Nano Lett. *19*, 8461–8468.

43. Xia, C., Zhu, P., Jiang, Q., Pan, Y., Liang, W., Stavitski, E., Alshareef, H.N., and Wang, H. (2019). Continuous production of pure liquid fuel solutions via electrocatalytic CO_2 reduction using solid-electrolyte devices. Nat. Energy *4*, 776–785.

44. García de Arquer, F.P., Dinh, C.-T., Ozden, A., Wicks, J., McCallum, C., Kirmani, A.R., Nam, D.-H., Gabardo, C., Seifitokaldani, A., Wang, X., et al. (2020). CO_2 electrolysis to multicarbon products at activities greater than 1 A cm^{-2}. Science *367*, 661–666.

45. Higgins, D., Hahn, C., Xiang, C., Jaramillo, T.F., and Weber, A.Z. (2019). Gas-diffusion electrodes for carbon dioxide reduction: a new paradigm. ACS Energy Lett. *4*, 317–324.